PROCEEDINGS OF SCIENCE

Stellar Intensity Interferometry observations at the Cherenkov Telescope Array Observatory with the Medium-Sized Telescopes

Quentin Luce,[a,*] **Jonathan Biteau,**[a,b] **François Brun,**[c] **Daniel Charlet,**[a] **Tarek Hassan,**[d] **Daniel Kerszberg**[e] **and Kevin Pressard** [a] **, on behalf of the CTAO-NectarCAM collaboration and SII science working group**

[a] *Université Paris-Saclay, CNRS/IN2P3, IJCLab, Orsay (France)*
[b] *Institut Universitaire de France (France)*
[c] *IRFU, CEA, Université Paris-Saclay, Gif-sur-Yvette (France)*
[d] *CIEMAT, Madrid (Spain)*
[d] *Sorbonne Université, CNRS/IN2P3, LPNHE, Paris (France)*

E-mail: quentin.luce@ijclab.in2p3.fr, jonathan.biteau@ijclab.in2p3.fr

The current generation of Imaging Atmospheric Cherenkov Telescopes (IACTs: HESS, VERITAS and MAGIC) has led to a renaissance in the use of stellar intensity interferometry for sub-milliarcsecond optical astronomy. This technique, used over distances of O(100 m) between telescopes, enabled the measurement of stellar radii on the order of a few hundred micro-arcseconds with a 10% resolution (assuming disk-like emission) for about 30 stars and binary systems. The new generation of IACTs, the Cherenkov Telescope Array Observatory (CTAO), is starting to follow this path. In particular, an SII observing system has been implemented in the camera of the prototype large-sized telescope at the CTAO North site, in conjunction with the MAGIC telescopes at La Palma (Spain). The larger the number and extent of the baselines, the better the angular resolution of SII measurements for smaller and/or fainter stellar objects. Thus, the addition of the medium-sized telescopes (MSTs) to SII observations at the CTAO sites will improve angular resolution to a few percent for the stars already measured. In addition, a relative precision comparable to that of previous generation IACTs will be achieved for a few hundred stars. SII observations with CTAO will also allow limb and gravity darkening, stellar ellipticity, etc., to be measured with a precision unattainable with previous generation IACTs.

But the larger the extent of the baselines, the more difficult it is to combine the signals from telescopes up to a kilometer apart. Previous SII projects with IACTs and hardware from radio interferometry experiments provide the necessary technology to equip the NectarCAM camera of the MSTs with an SII observing system. Two technological solutions are investigated. One is a digital acquisition system integrating an improved WhiteRabbit node (IDROGEN), and the other is an analog acquisition system based on a vertical cavity surface emitting laser employed in the current-generation gamma-ray observatories. The first tests performed do not prefer one solution from the other.

39th International Cosmic Ray Conference (ICRC2025)
15–24 July 2025
Geneva, Switzerland

*Speaker

PoS(ICRC2025)736

1. Introduction

1.1 Stellar Intensity Interferometry

Nowadays the best technique for resolving objects in the sky involves combining light observed by telescopes separated from each other by hundred of meters or more. In the optical domain, two techniques were developed mainly in the 20$^{\text{th}}$ century and are now referred to as amplitude (or phase) interferometry and intensity interferometry. Amplitude interferometry, developed at the beginning of the 20$^{\text{th}}$ century, records the interference fringes created by combining light from different telescopes. The basic measurements are the amplitude (or height) of the fringes and the phase (or the position of the peak in the fringe pattern). The former enables to compute the fringe contrast, often called the "visibility" of the fringes. This visibility evolves with the distance between the two telescopes, forming a visibility curve. In interferometry theory, this curve is related to the first-order correlation function $g^{(1)}(d)$, where d is the separation, or baseline between the two telescopes.

Intensity interferometers correlate the fluctuations of the light recorded at different telescopes without physically combining the two light beams. Intensity interferometry, developed by R. Hanbury Brown, and theorized by R.Q. Twiss, gives access to the second-order correlation, $g^{(2)}(d)$, related to the square of the visibility curve. In the 60's, the first generation of intensity interferometers was built in Australia (Narabrii Stellar Intensity Interferometer) to observe stellar sources with a sub-milliarcsecond (mas) resolution at blueish wavelengths. This led to the measurements of the stellar radii of 32 stars (with apparent magnitude < 2.5) assuming that the stars are uniform disks objects [1].

However, intensity interferometry has a poor signal-to-noise ratio and requires fast electronics, nanosecond time accuracy, observations through narrow-band filters, and several telescopes with a large collecting areas. After being almost forgotten for half a century, efforts were made at the beginning of the 21$^{\text{st}}$ century [2] to demonstrate that Imaging Atmospheric Cherenkov Telescopes (IACTs) fulfill these requirements and are suitable observatories for hosting Stellar Intensity Interferometry (SII) programs. Thus, over the past decade, the latest generation of IACTs, including H.E.S.S., MAGIC and VERITAS, has conducted SII observations on bright nights when γ-ray observations, for which IACTs were designed, are not possible. Recent results have been published, measuring 30 stellar radii with 10% precision [3], at different wavelengths [4] and studying the complex dynamic of stars [5]. The Cherenkov Telescope Array Observatory (CTAO), a new array of IACTs under construction, is expected to surpass the limits of current IACTs in γ-ray observations but could also usher in a new era of optical astronomy by implementing a SII program.

1.2 Cherenkov Telescope Array Observatory

Designed for γ-ray observations, CTAO detects short blue flashes of Cherenkov light emitted by the atmospheric cascade of secondary particles. To provide full-sky access, the CTAO is separated into two sites of observations. In the northern hemisphere, at La Palma (Canary Island, Spain) at an altitude of 2.2 km, CTAO-N is dedicated to GeV-TeV observations. The northern array includes 4 Large-Sized Telescopes (LSTs), each with a mirror area of 370 m^2 and 9 Medium-Sized Telescopes (MSTs), each with a mirror area of 88 m^2. The CTAO-N site covers an area of ~0.25 km^2 as depicted in Fig. 1-left. In the southern Hemisphere, the CTAO-S, located at the Paranal Observatory in Chile,

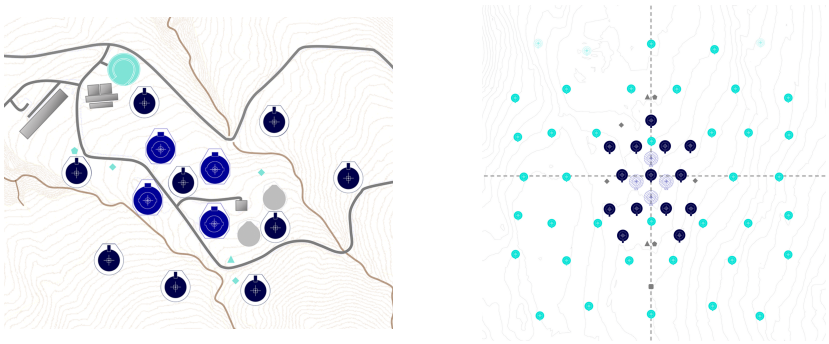

Figure 1: *Left*: Layout of the CTAO northern site, for which the maximum distance between two telescopes is 560 m. *Right:* Layout of the CTAO southern site, for which the maximum distance between two telescopes is 2500 m. The blue, dark blue and cyan markers represents respectively the position of the LSTs, of the MSTs and of the SSTs.

will observe γ-rays with energies ranging from 150 GeV to 300 TeV. It will consist of 14 MSTs and 37 Small-Sized Telescopes (SSTs) with a mirror area of ~8 m^2, thus covering an array of ~3 km^2 (see Fig. 1-right). In addition to the large number of pairs of telescopes (78 for the CTAO-N and 1,275 for the CTAO-S) that can be used to correlate the fluctuations of intensity from stars, the maximum baselines of these telescope layouts are ~600 m for CTAO-N and ~2.5 km for CTAO-S. This makes them outstanding observatories for SII observations of sub-mas objects.

At the time of writing, the prototype LST of the CTAO-N is equipped with an operational SII system [6, 7]. A dedicated SII system is being designed and tested for the MSTs of the CTAO-N and the SSTs of the CTAO-S, and discussions are ongoing for the MSTs of the CTAO-S.

In these proceedings, we focus on the expected performances that CTAO could achieve in measuring stellar radii with a SII program implemented at both the Northern and Southern sites (Sec. 2), while the broader prospects for SII science with the CTAO are presented in [8]. In Sec. 3, we discuss the program under testing to perform SII observations with the MSTs of CTAO-N and with its camera, the NectarCAM [9]. Each NectarCAM camera is composed of 1,855 photomultiplier tubes (PMTs), grouped into modules of 7 PMTs, each of which is controlled by a Front-End Board (FEB) and connected to the rest of the camera through a Back-Plane (BP). Each pixel or PMT of the camera has a field-of-view of ~0.18° = 6.48×10^5 mas and only a couple of pixels per camera are equipped for SII observations.

2. Measurements of stellar radii and limb-darkening coefficient

2.1 Simulation of the squared visibility curve for a star

The design of the telescopes and the selected layouts for the α-configuration of the CTAO further push the limits of SII observations with IACTs. The measurement of the stellar radii is the first achievable science case and is expected to reach an unprecedented level of precision. Quantifying these performances requires simulating the squared visibility curve of an observed star with an apparent magnitude in the B-band, m_B, and a diameter, θ_B.

Except for the LSTs at the northern site, the system dedicated to SII observations is still under development and testing for the MSTs and SSTs. Thus some contributions, such as the response of

the instrument's response modified to perform SII observations, are still being studied and are not, or only partially, included in the simulations.

An intensity interferometer measures the components of the sky Fourier transform by sampling the squared visibility curve $|V(\lambda, d)|^2$, where λ is the wavelength at which the observations are performed, and d is the baseline between telescopes. According to the model developed in [10], the squared visibility curve can be expressed as follows:

$$|V(\lambda, d)|^2 = \left(\frac{1-u_\lambda}{2} + \frac{u_\lambda}{3}\right)^{-2} \left[(1-u_\lambda)\frac{J_1(x)}{x} + u_\lambda\sqrt{\frac{\pi}{2}}\frac{J_{3/2}(x)}{x^{3/2}}\right]^2 \quad (1)$$

where $x = \pi\theta_{\rm LD}d/\lambda$, and $J_1(x)$ and $J_{3/2}(x)$ are the Bessel functions of the first kind. In this expression, the star is not described as a uniform disk, but rather as exhibiting a limb-darkening effect, which is a gradual decrease in observed surface intensity from the center to the edge of the star. For example, depending on the model used, the intensity at the edge of the Sun's disk is ~20-30% of the intensity at its center, at a wavelength of 550 nm. This effect is described by the limb-darkening coefficient u_λ. The larger the value of u_λ, the larger is the limb-darkening effect. When $u_\lambda = 0$, Eq. 1 simplifies to the uniform disk model. For the remainder of this paper, we denote $\theta_{\rm UD}$ as the angular diameter of a star modeled as a uniform-disk and $\theta_{\rm LD}$ as the angular diameter of a limb-darkened star.

At a given baseline, i.e., when considering a specific pair of telescopes observing a star, the signal-to-noise ratio is expressed as:

$$S/N = A\alpha(\lambda)q(\lambda)n(\lambda)F^{-1}\sigma\sqrt{b_\nu}\,|V(\lambda, d)|^2\sqrt{\frac{T}{2}}\,[(1+a)(1+\delta)]^{-1}\,, \quad (2)$$

where A is the mirror area, $\alpha(\lambda)$ is the quantum efficiency of the PMT, $q(\lambda)$ is the optical efficiency of the telescope (including the reflectivity of the mirror, transmission through the window of the camera, etc.) and $n(\lambda)$ is the differential photon flux of the observed star of magnitude m_B. F is the excess noise factor of the PMT, $b_\nu = 500$ MHz is the cross-correlation electrical bandwidth, T is the observing time and σ is the normalized spectral distribution of the optical passband. In the performed simulation, the considered optical passband is a narrow band centered at a wavelength of 425 nm with a width of 26 nm.

The parameters a and δ characterize additional noise coming from the correlator/electronics and background light, respectively. Currently, the amount of noise added by the correlator/electronics is unknown and has been fixed such that $1/(1+a) = 0.7$. Stellar observations with IACTs are scheduled during bright nights. For the CTAO, these nights are defined as nights when the background photon rate is equivalent to ten times the photon rate of the Night Sky Background (NSB). In the B-band, the equivalent magnitude of the NSB in a field-of-view ~0.18°, is $m_{\rm NSB}$ ~9, so the equivalent magnitude of ten times the NSB is $m_{10\times{\rm NSB}}$ ~6.5. According to the moonlight model in [11], these requirements are met during Moon phases when the fraction of the Moon illuminated is at least 25%, provided that the Moon and the observed star are sufficiently separated. In our simulations, we assume that the background Moonlight is equivalent to a star in the pixel's field-of-view with a magnitude of $m_B = 6$.

The last relevant parameters of Eq. 2 are for the LST, MST and SST, $\alpha(\lambda) = 0.39, 0.39, 0.58$, $q(\lambda) = 0.62, 0.65, 0.65$ and F =1.21, 1.21, 1.03, respectively. It is important to note that these

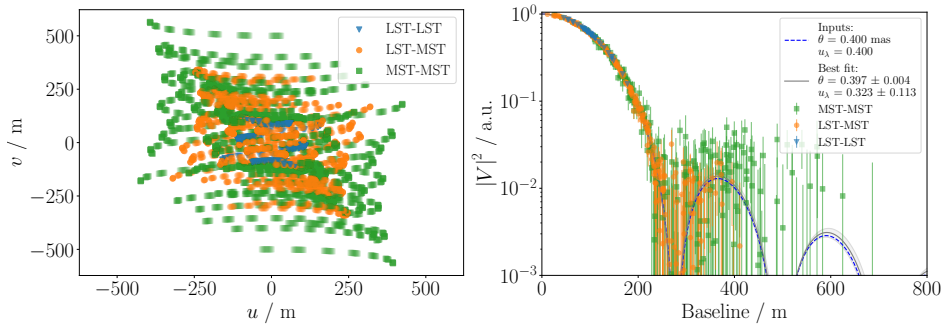

Figure 2: *Left:* Example of a *(u,v)*-coverage for a simulation of a star observed, at the Northern site, 20 minutes every night during 7 nights. Each point represent the average *(u,v)*-position for an observation time of 1 minute and for a particular pair of telescopes. For the sake of clarity the pairs of telescopes have been regrouped in LST-LST, LST-MST and MST-MST pairs. *Right:* Example of a squared visibility curve as a function of the baseline for a star observed at the Northern site with a magnitude $m_B = 2$, a diameter $\theta_B = 0.4$ and presenting a linear limb-darkening coefficient $u_\lambda = 0.4$.

values are preliminary and may evolve in the future. Indeed, the program to equip the SSTs is still in the design phase. To simplify the discussions in these proceedings, we consider the SST as a *small* MST with a SiPM. This explains why the quantum efficiency and excess noise factor differ, while other parameters remain similar or are adapted to the geometry of the SST. The observing time is split into 7×20 minutes periods over 7 consecutive nights, which increases the coverage in the *(u,v)*-plane of the sky Fourier transform. The resulting coverage is presented in Fig. 2-left for a simulation performed at CTAO-N.

Since the information of the geometry and dynamics of the star are encompassed in the resulting squared visibility sampled at a fixed position in the *(u,v)*-plane, a large and dense coverage probes more features of the stars as the observed signal is still distinguishable from the background noise. Figure 2-right shows an example of a squared visibility curve for a star with a diameter of $\theta_B = 0.4$ mas, a magnitude of $m_B = 2$ and a limb-darkening coefficient of $u_\lambda = 0.4$, as observed at the CTAO-N. The designed layout limits the correlation of intensity fluctuations of pairs of LSTs at baselines ≤ 200 m. When the MSTs are added, the second lobe of $|V|^2$ is probed, but with larger uncertainties as shown by the results of the best-fit for this example. The fainter and/or smaller the star, the large the uncertainties at larger baselines.

2.2 Stars for stellar intensity interferometry observations

A recent catalog of stars targets for SII observations has been released through a web application [12]. It contains 9,110 from the Yale Bright Star Catalog. 3,100 of those stars have enough information for the application's purposes.

To evaluate the performances of the CTAO in measuring stellar radii, stars of magnitudes $m_B \leq 6$ were simulated. Two tests have been conducted for each star. The first one models the star as a uniform disk. This test has two free parameters: the diameter of the star θ_{UD}, and the zero-baseline correlation normalization, which is fixed at 1 during the simulation process and left free during reconstruction. The second test models the star affected by the limb-darkening effect with a coefficient $u_\lambda = 0.4$. In this test, three parameters are free: the diameter θ_{LD}, the

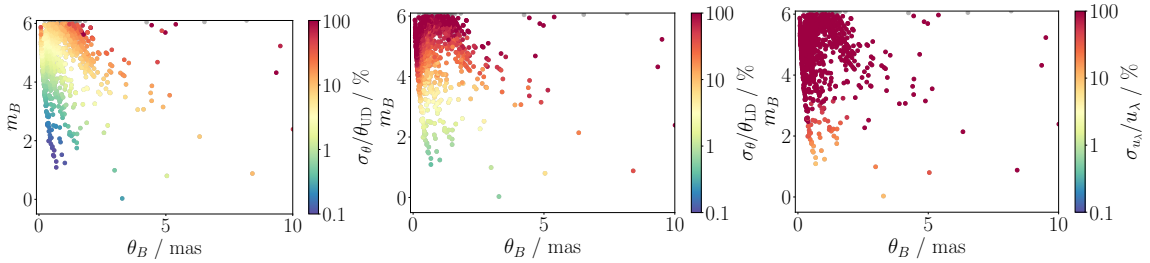

Figure 3: Population of stars observable at CTAO-N. The z-color scale represents the expected resolution for the reconstruction of the diameter of the star following a uniform-disk model $\theta_{\rm UD}$ (*left*), following a limb-darkening model $\theta_{\rm LD}$ (*middle*) and for the reconstruction of the linear limb-darkening coefficient u_λ (*right*).

coefficient u_λ, and the zero-baseline correlation normalization. The expected performances for the CTAO-N on the precision of reconstructing $\theta_{\rm UD}$, $\theta_{\rm LD}$ and u_λ are presented in Fig. 3. Describing stars as uniform disks, the CTAO-N reconstructs the diameter $\theta_{\rm UD}$ with a precision better than 1% for stars with a magnitude $m_B \lesssim 4$ and a diameter $\theta_{\rm UD} \lesssim 1.5$ mas, representing nearly 200 hundred stars observables. Using the CTAO-S layout, the radii of fewer than 100 stars can be measured with a precision better than 1%. In the CTAO-S, adding the MSTs in the layout available for SII observations increases the number of stars observable with such precision by enabling the observation of fainter stars with diameters of $\theta_{\rm UD} \lesssim 1.5$ mas. Without the MSTs, the measurements are limited to small but bright stars in the sky, for which the first lobe of the $|V|^2$ extends to baselines of 400-500 m, dividing by ~3 the number of star reachable with such precision.

The same procedure is applied to simulate limb-darkened stars with a coefficient $u_\lambda = 0.4$. In this case, both the diameter of the star and the limb-darkening coefficient are free parameters, resulting in the reconstruction of the profile of less than 50 stars with a precision better than 2% (and less than 100 stars with a precision better than 5%). These are bright stars ($m_B \lesssim 2$) for which the limb-darkening coefficient is constrained with a precision better than 25%. The results presented in this section are comparable to those obtained from simulations with different values of u_λ. However for values $u_\lambda \lesssim 0.2$ of the limb-darkening coefficient, constraining it with a precision better than 20% is achieved for brighter stars ($m_B \lesssim 0.5$) only. Finally, for the CTAO-S, MSTs are required to achieve a precision of $u_\lambda < 50\%$ for ~20 stars.

3. Implementation of a SII system in the NectarCAM

As mentioned previously, SII observations with IACTs are a complementary project that extends the duty-cycle of the telescopes during bright nights when γ-ray observations are difficult. Additionally, the philosophy followed by the SII group is to keep the modifications of the telescope/camera minimal, at least during a first implementation phase, to avoid interfering with the standard equipments.

The NectarCAM group adopted a system similar to that implemented in the MAGIC telescopes [3] and in the LST. The NectarCAM possesses a calibration system that uses a white screen and a flasher to calibrate the gain of the PMTs as described in [13]. The screen is placed in front of the PMTs and can be moved to different positions to reach the 1855 pixels of the camera. We

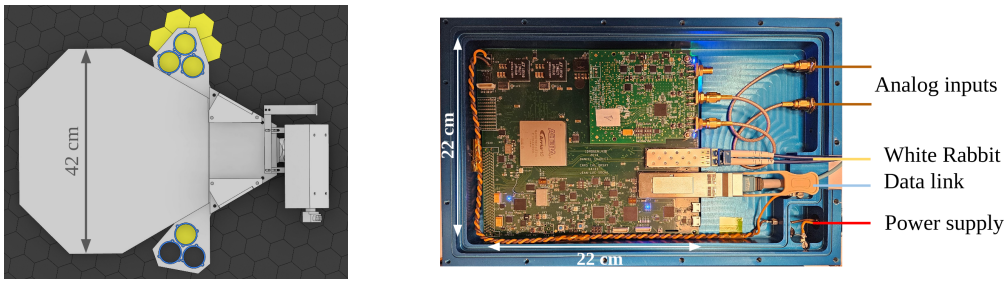

Figure 4: *Left:* Scheme of the modifications made to the support of the calibration screen of the NectarCAM to add 6 narrow-band filters. *Right:* Picture of the IDROGEN board.

use this device to support the optical filters that need to be placed in front of the PMTs during SII observations. Figure 4-left shows a rendering of the white screen and the support for the six optical filters. Currently, we use Semrock filters with a band centered at a wavelength of 425 nm with a width of 26 nm. There are ongoing discussions to used different optical filters with narrower bands to detect, for example, the emission lines H-β $\sim$ 486 nm and H-α $\sim$ 434 nm. In [3], the main source of systematic uncertainties comes from the background subtraction. One way to reduce these uncertainties is to place the screen in front of multiple pixels with the same optical passband filter. One pixel will point to the selected star, and the other will look slightly off-center to better estimate the background. To extract the signal of the anode of these ON-star pixel, the corresponding FEB and BP have been modified such that a connection has been added on the FEB and SMA outputs have been implemented on the BP.

The main challenge with SII observations is the transmission of the signal to a computing system that digitizes and correlates the signal from all pairs of telescopes. Two technological solutions are being investigated. One solution is a digital acquisition system that integrates an improved WhiteRabbit node, IDROGEN [14], and is placed directly in the camera. A picture of the board is presented in Fig. 4-right. This version of the board supports two analog input signals and samples each at a rate of 1 GS/s, sending data through 10 GB optical links. In addition to continuous sampling of the signal (with or without a defined threshold), the IDROGEN board is well suited for photon tagging and can directly compute Fourier transformation. These boards are already implemented in the PAON IV radio-interferometers, acting as prototypes for the Tianlai project. The other solution is an analog transmission system over hundred of meters or kilometers. It is based on a vertical cavity surface emitting laser employed in the current-generation γ-ray observatories. In this case, the digitization of the analog signal is performed by the computing system hosting the correlator [3]. As a preliminary test to compare the different options, the signal of 1 photo-electron generated by a flasher is analyzed. The results are presented in Fig. 5 for the IDROGEN board with a direct digitization, for the system implemented in the LST telescopes and for an industrially manufactured system with a transmission over 300 m before digitization. The initial tests do not show noticeable alterations of the signal from one device compared to another. Note that the undershoot observed in Fig. 5 for the IDROGEN acquired signal is under treatment and will be compensated for in later versions of the IDROGEN board.

As a final remark, the expected volume of data assuming a continuous recording of the fluctuations of the intensity during 2.5 hours, is of the order of several tens of TB per MST at the

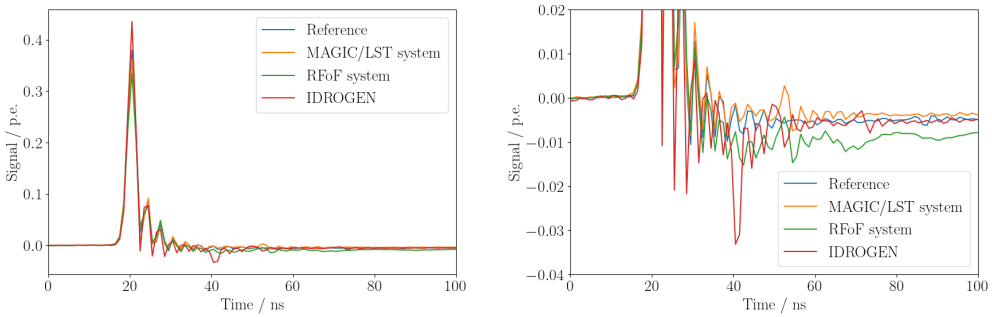

Figure 5: *Left:* Example of the signal observed by one SII-modified pixel of the NectarCAM in blue, after transport over 300 m and digitization using a LST-like system in orange, after transport over 300 m and digitization using a RF-over-fiber industrial system in green and after a digitization using the IDROGEN board in red. *Right:* Zoom over the signal of the left panel.

CTAO-N. In case of an on-line correlation of the signals of each telescope, having a digitization of the signal at the back of the camera will significantly decrease the computational resources needed at the correlator site.

4. Conclusion

The revival of Stellar Intensity Interferometry with IACTs is opening a new window on sub-milliarcsecond astronomy. The dense and large coverage in *(u.v)*-plane allows observations of stellar geometry and dynamics with an unprecedented precision, on top of increasing the number of stars reachable. As an example, we have shown that the limb-darkening coefficient is expected be measured with a 20% precision for dozens of identified stars.

As for the implementation of a SII system, the NectarCAM group in charge of the development of the camera of the MST at CTAO-N is testing several options for the transmission/digitization of the signal of the PMT. Future tests are scheduled to push the limits of each options and will be presented in further contributions.

References

[1] R. Hanbury Brown et al., *MNRAS* (1974) **167** 121-136.
[2] D. Dravins and S. LeBohec, Proceedings of SPIE **6986** 698609 (2008).
[3] S. Abe et al. [MAGIC Coll.], *MNRAS* (2024) **529**, 4387–4404, [2402.04755].
[4] N. Vogel et al., *MNRAS* (2025) **537**, 2334–2341, [2411.16471].
[5] A. Acharyya et al. [VERITAS Coll.], *ApJ* **966** (2024) 28, [2401.01853].
[6] I. Jiménez Martínez et al., PoS(ICRC2025)**XXX**.
[7] A. Raiola, PoS(ICRC2025)**XXX**.
[8] P. Saha et al., PoS(ICRC2025)**XXX**.
[9] J-F. Glicenstein et al. [CTAO Consortium.], PoS(ICRC2015)**937**, [1508.06555].
[10] R. Hanbury Brown et al., *MNRAS* (1974) **167** 475-484.
[11] K. Krisciunas and B.E. Schaefer, *PASP* **103** (1991) 1033.
[12] L. Stanic et al., Stars available for Intensity Interferometry (2024), web application.
[13] B. Biasuzzi et al., *NIM A* **950** (2020) 162949, [1910.07446].
[14] D. Charlet et al., *13^{th} White Rabbit Workshop*, CERN, (2024)